

Non-desolvation Zn^{2+} storage mechanism enables MoS_2 anode with enhanced interfacial charge-transfer kinetics for low temperature zinc-ion batteries

Zeheng Lv¹, Yu Tan², Yuanhong Kang¹, Jin Yang¹, Xian Cheng³, Weiwei Meng⁴, Yufei Zhang³, Cheng Chao Li^{3*}, Jinbao Zhao^{1*} & Yang Yang^{1*}

¹State Key Laboratory of Physical Chemistry of Solid Surfaces, State-Province Joint Engineering Laboratory of Power Source Technology for New Energy Vehicle, College of Chemistry and Chemical Engineering, Xiamen University, Xiamen 361005, China;

²College of Materials Science and Engineering, Hunan University, Changsha 410082, China;

³School of Chemical Engineering and Light Industry, Guangdong University of Technology, Guangzhou 510006, China;

⁴State Key Laboratory of Vanadium and Titanium Resources Comprehensive Utilization, Panzhihua 617000, China

Received December 30, 2022; accepted February 27, 2023; published online April 17, 2023

The emerging rocking-chair aqueous zinc-ion battery (AZIB) configuration provides a promising approach for realizing their practical applications by avoiding the critical drawbacks of Zn metal anodes including unsatisfactory Coulombic efficiency and low Zn utilization. Therefore, exploiting appropriate insertion-type anodes with fast charge-transfer kinetics is of great importance, and many modifications focusing on the improvement of electron transport and bulk Zn^{2+} diffusion have been proposed. However, the interfacial Zn^{2+} transfer determined by the desolvation process actually dominates the kinetics of overall battery reactions, which is mainly overlooked. Herein, the interlayer structure of MoS_2 is rationally co-intercalated with water and ethylene glycol (EG) molecules ($\text{MoS}_2@\text{EG}$), giving rise to a fast non-desolvation Zn^{2+} storage mechanism, which is verified by the extraordinarily smaller activation energy of interfacial Zn^{2+} transfer (4.66 kJ mol^{-1}) compared with that of pristine MoS_2 ($56.78 \text{ kJ mol}^{-1}$). Furthermore, the results of theoretical calculations, *in-situ* Raman and *ex-situ* characterizations also indicate the enhanced structural integrity of $\text{MoS}_2@\text{EG}$ during cycling due to the enlarged interlayer spacing and charge screening effect induced by interlaminar EG molecules. Consequently, the $\text{MoS}_2@\text{EG}$ anode enables excellent cycling stability of both high-energy-density $\text{MoS}_2@\text{EG}||\text{PVO}$ (polyaniline intercalated V_2O_5) and high-voltage $\text{MoS}_2@\text{EG}||\text{Na}_3\text{V}_2(\text{PO}_4)_2\text{O}_2\text{F}$ (NVPF) full batteries with neglectable capacity decay at -20°C .

rocking-chair aqueous zinc-ion battery, insertion-type anode materials, non-desolvation Zn^{2+} storage mechanism, charge screening effect, layered MoS_2 anode

Citation: Lv Z, Tan Y, Kang Y, Yang J, Cheng X, Meng W, Zhang Y, Li CC, Zhao J, Yang Y. Non-desolvation Zn^{2+} storage mechanism enables MoS_2 anode with enhanced interfacial charge-transfer kinetics for low temperature zinc-ion batteries. *Sci China Chem*, 2023, 66, <https://doi.org/10.1007/s11426-022-1556-x>

1 Introduction

Aqueous rechargeable Zn-ion batteries (ZIBs) with Zn metal as anode have shown considerable potential in next-

generation large-scale electrochemical energy storage applications due to the outstanding merits of low cost, environmentally friendly and inherent high safety. To date, various cathode materials including Prussian blue analogues, manganese oxides, vanadium-based materials and organic cathodes have been developed and achieved impressive Zn^{2+} storage performance [1–3]. Despite the high theoretical ca-

*Corresponding authors (email: licc@gdut.edu.cn; jbzhao@xmu.edu.cn; yangyang419@xmu.edu.cn)

capacity (820 mAh g⁻¹) and relatively low redox potential (-0.763 V vs. SHE) of Zn, there are still severe challenges on the Zn metal anode side in terms of low Coulombic efficiency (CE) and limited Zn utilization.

First, the Zn-metal anode is inevitably faced with the issues of the continuous formation of zinc dendrites caused by inhomogeneous Zn²⁺ flux at the electrode/electrolyte interface. Another weakness is that the interface between Zn metal and aqueous electrolyte is thermodynamically unstable, resulting in detrimental hydrogen evolution reaction (HER) and self-corrosion side reactions. In order to address those scientific challenges, numerous efforts toward interfacial protective layer and three-dimension (3D) electrode design have been devoted to improving the reversibility of Zn-metal anode [4–12]. In addition, other modification strategies focused on stabilizing electrode/electrolyte interface have been also reported. It is proposed that using high-concentration electrolyte or designing electrolyte additives could lower the content of free water and optimize Zn²⁺-solvation-sheath structure in electrolyte [13–15], thus inhibiting the hydrogen evolution reaction. Despite this great progress, the CE of these modified Zn metal anode is usually lower than 99.6%, which still fails to meet the requirements of actual battery system (>99.9%). The lower CE implies that a great amount of excessive Zn is necessary to compensate for the irreversible loss during cycling, which will definitely reduce the energy density of batteries.

Most recently, a novel “rocking-chair” ZIB is recommended by using Zn²⁺ storage materials with a relatively low working potential to replace Zn metal anodes. Our group [16–18] has previously demonstrated that such an innovation configuration can not only avoid the formation of Zn dendrites fundamentally but also enhance the CE by eliminating interfacial parasitic side reactions. Among various types of anode materials for ZIBs, the research on conversion and organic anodes is still at the beginning [2,16,19–21]. Based on the successful commercialization experience of graphite anodes for lithium-ion batteries, it is reasonable to predict that insertion-type electrodes should be the most promising anodes including Mo₆S₈, Zn₂Mo₆S₈, TiS₂, Na_{0.14}TiS₂, MoO₂, α-MoO₃, h-MoO₃, WO₃, NHVO@Ti₃C₂T_x ((NH₄)₂V₁₀O₂₅·8H₂O@Ti₃C₂T_x), Zn_xMo_{2.5+y}VO_{9+z}, TiSe₂ and Cu_{2-x}Se [17,18,22–32]. Nonetheless, exploiting appropriate insertion-type anode materials with fast charge-transfer kinetics is still challenging, and many modifications are mainly focused on the improvement of electron transport and bulk Zn²⁺ diffusion.

Analyzing Zn²⁺ storage kinetics in conventional anode materials systematically, the reaction is composed of several basic processes: (1) solvated Zn²⁺(H₂O)₆ diffusion between positive and negative electrodes through an aqueous electrolyte; (2) the removing of Zn²⁺(H₂O)₆ solvation sheath at electrode/electrolyte interface accompanied by the transfer

of electrons; (3) the diffusion of naked Zn²⁺ ions inside active materials. Generally, the electron transport is ensured to be much faster than Zn²⁺ transport by adding conductive agents. Moreover, the desolvation process is generally accepted to be the rate-determined process rather than Zn²⁺ diffusion process in bulk structure, due to the strong coordination environment between Zn²⁺ and H₂O. Therefore, the development of fast interfacial charge-transfer mechanism with low desolvation penalty may be an ultimate route to realize the application of advanced anode materials with rapid charge/discharge abilities [33–36].

Herein, for the first time, the novel MoS₂@EG anode is successfully prepared *via* co-intercalating water and ethylene glycol (EG) molecules into the interlayer structure of MoS₂. Through Arrhenius equation, it is found that MoS₂@EG anode shows extremely low activation energy of interfacial Zn²⁺ transfer (4.66 kJ mol⁻¹) but 56.78 kJ mol⁻¹ for MoS₂ (Figure 1c, d, Figure S6, Supporting Information online), indicating the solvated Zn²⁺(H₂O)₆ may intercalate into MoS₂@EG for avoiding the complex desolvation process with high charge-transfer resistance (Figure 1a, b). Thus, it is believed that the MoS₂@EG anode possesses the desired electrochemical energy storage characteristics of fast non-desolvation Zn²⁺ storage mechanism. As a result, the MoS₂@EG anode with enhanced interfacial charge-transfer kinetics can boost the construction of long lifespan and low temperature rocking chair ZIBs.

2 Materials and method

2.1 Materials synthesis

2.1.1 Synthesis of MoS₂@H₂O

The MoS₂@H₂O was synthesized by a reported hydrothermal reaction. Firstly, 0.412 g (NH₄)₆Mo₇O₂₄·4H₂O and 0.355 g CH₄N₂S (thiourea) were added into 55 mL deionized water to form a clear solution. Then, the mixture was transferred into a 100 mL autoclave with Teflon-liner to treat at 170 °C in an oven. After 24 h, the product was washed with deionized water and absolute ethanol to remove the impurities. Finally, the above product was dried at 60 °C in vacuum for 12 h and the black MoS₂@H₂O powder can be obtained.

2.1.2 Synthesis of MoS₂

The pure MoS₂ was prepared *via* treating the MoS₂@H₂O powder at a 400 °C N₂ flow for 3 h.

2.1.3 Synthesis of MoS₂@EG

The MoS₂@EG was prepared through modifying the synthetic route of the above MoS₂@H₂O moderately. 0.412 g (NH₄)₆Mo₇O₂₄·4H₂O and 0.355 g CH₄N₂S (thiourea) were added into the mixture containing 40 mL deionized water

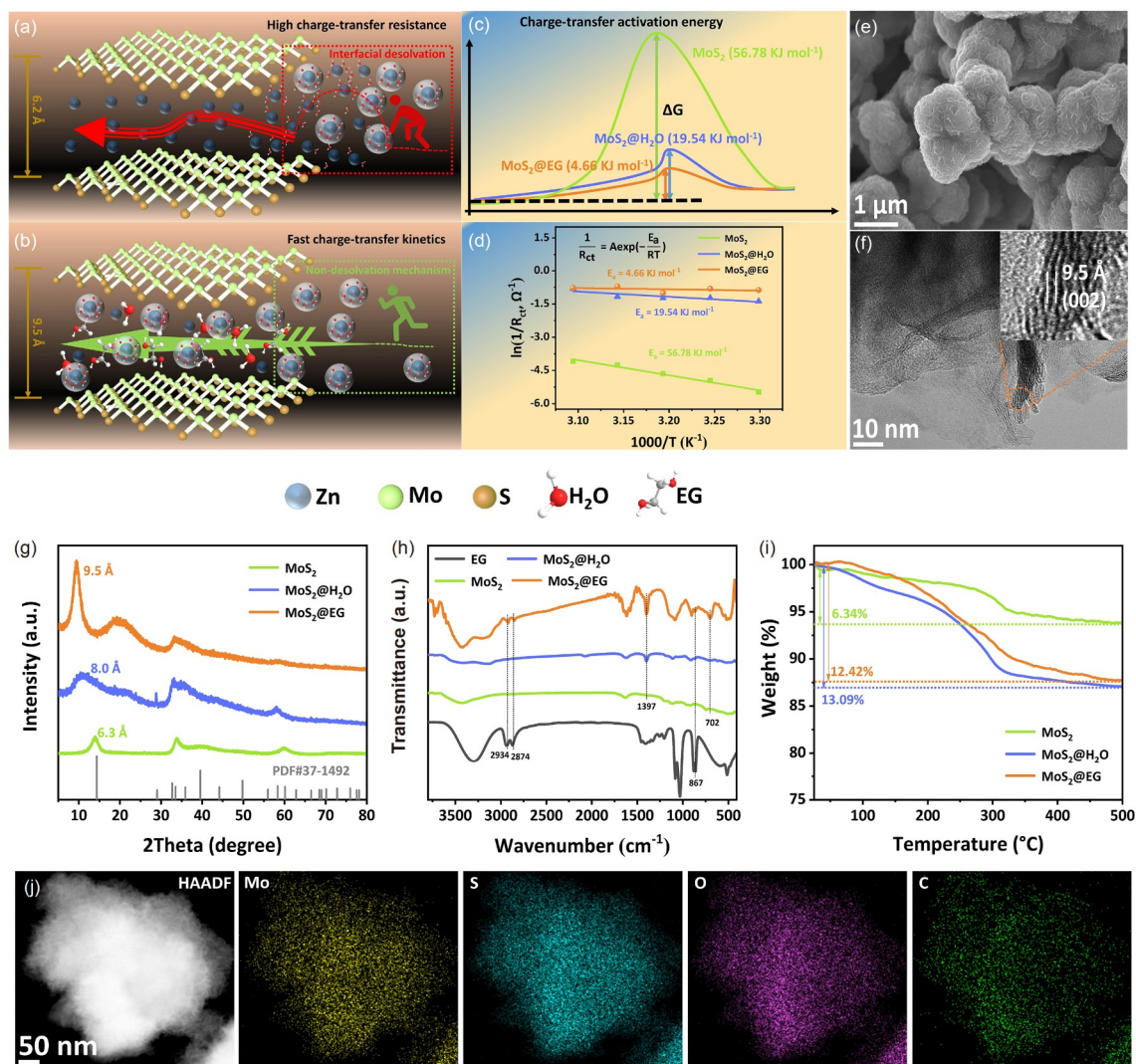


Figure 1 The schematic diagram of the charge storage mechanism of (a) MoS_2 and (b) $\text{MoS}_2@\text{EG}$. (c, d) The calculated desolvation activation energies of MoS_2 , $\text{MoS}_2@\text{H}_2\text{O}$ and $\text{MoS}_2@\text{EG}$ by using Arrhenius equation. (e) The SEM image of $\text{MoS}_2@\text{EG}$. (f) HR-TEM images of $\text{MoS}_2@\text{EG}$. (g) The XRD results of MoS_2 , $\text{MoS}_2@\text{H}_2\text{O}$ and $\text{MoS}_2@\text{EG}$. (h) FTIR curves of EG, MoS_2 , $\text{MoS}_2@\text{H}_2\text{O}$ and $\text{MoS}_2@\text{EG}$. (i) TGA profiles of MoS_2 , $\text{MoS}_2@\text{H}_2\text{O}$ and $\text{MoS}_2@\text{EG}$. (j) High-angle annular dark-field image and corresponding elemental mapping of the $\text{MoS}_2@\text{EG}$ (color online).

and 15 mL ethylene glycol to form a homogeneous solution. Then the same process as $\text{MoS}_2@\text{H}_2\text{O}$ was carried out to get the final $\text{MoS}_2@\text{EG}$ powder.

2.1.4 Synthesis of polyaniline intercalated V_2O_5 (PVO)

The 0.2 g commercial V_2O_5 powder and 30 mL deionized water were mixed with magnetic stirring, and then 60 μL aniline was added into the mixture to form a homogeneous solution. After 30 min, the pH of the above solution was adjusted to 3 with 3 M HCl. Finally, the PVO can be obtained after reacting at 120 $^\circ\text{C}$ for 24 h in a 50 mL autoclave with Teflon-liner.

2.1.5 Synthesis of $\text{Na}_3\text{V}_2(\text{PO}_4)_2\text{O}_2\text{F}$ (NVPF)

With the molar ratio of 1:3, V_2O_5 and $\text{H}_2\text{C}_2\text{O}_4$ were dispersed evenly in deionized water at 70 $^\circ\text{C}$. Next, $\text{NH}_4\text{H}_2\text{PO}_4$ and

NaF with stoichiometric ratios were added and the pH of the mixed solution was adjusted to 7 with ammonia subsequently. After that, the mixture was heated at 170 $^\circ\text{C}$ in oven. After 12 h, the NVPF product can be collected.

2.2 Material characterization

X-ray diffraction (XRD) (D8 ADVANCE, Bruker, Germany) was utilized to determine the crystalline structures. Scanning electron microscope (SEM) images were got using a SU8220 (Hitachi, Japan). Transmission electron microscope (TEM) images were obtained by Talos F200S (FEI, Thermo, Czech, USA). X-ray photoelectron spectroscopy (XPS) was characterized by Escalab 250Xi (Thermo Fisher, USA). FTIR spectra were collected by a FTIR spectrometer (Nicolet iS5, Thermo Scientific). Thermogravimetric (TGA, STA449F5,

Netzsch, Germany) measurement was implemented from room temperature to 500 °C under a nitrogen flow at 10 °C min⁻¹ heating rate. *In situ* electrochemical Raman spectra were tested *via* LabRAM HR Evolution (HORIBA FRANCE).

2.3 Electrochemical measurement

Firstly, the active material (MoS₂, MoS₂@H₂O or MoS₂@EG), carbon black and polyvinylidene fluoride (PVDF) with a mass ratio of 7:2:1 were mixed evenly in *N*-methyl-2-pyrrolidone (NMP) to form homogeneous slurry. Then the mixture was pasted onto the carbon cloth and dried at 80 °C for 12 h in the vacuum oven. The loading mass of active material in electrodes was about 3.0–4.0 mg cm⁻². With 3 M Zn(CF₃SO₃)₂ electrolyte, Glass fiber filter (GF-D, Whatman) separator, Zn counter electrode and working electrode, the CR-2032 type coin half-cells were assembled for electrochemical tests.

Secondly, through the same crafts as working electrodes (as a part of the fabrication of full cell, the current collector of MoS₂@EG was copper foil), the NVPF and PVO cathode materials were pasted onto a carbon cloth and dried at 80 °C for 12 h in the vacuum oven, respectively. The loading mass of NVPF and PVO was about 12.0–14.0 mg cm⁻² and 4.0–6.0 mg cm⁻², respectively. Before the fabrication of CR-2032 type coin full-cells, the NVPF cathode was paired with Zn foil to be assembled into a half-cell with a subsequent electrochemical cycling at 0.1 A g⁻¹ between 0.6 and 2.0 V for 10 cycles and then the half-cell was discharging at the constant voltage of 0.6 V for 32 h to obtain the Zn²⁺ pre-intercalated Zn_xNVPF cathode. Similarly, the Zn²⁺ pre-intercalated Zn_xPVO cathode was prepared through the processes of activating PVO at 0.2 A g⁻¹ between 0.2 and 1.6 V for 4 cycles and then the PVO||Zn half-cell was discharging to 0.2 V at 0.2 A g⁻¹. According to different electrochemical characteristic of Zn_xNVPF and Zn_xPVO, the electrolyte for MoS₂@EG||Zn_xNVPF and MoS₂@EG||Zn_xPVO was 4 M and 3 M Zn(CF₃SO₃)₂, respectively.

The galvanostatic charge-discharge tests were implemented on the Neware battery system. Cyclic voltammetry (CV) and electrochemical impedance spectroscopy (EIS) tests were conducted by using the electrochemical workstation (Interface 1010B, Gamry).

2.4 Theoretical calculations

The Vienna Ab Initio Simulation Package (VASP) was utilized to measure all first-principles calculations based on the foundation of density functional theory (DFT). The geometry optimizations were carried out to make the forces apply on the ions less than 0.02 eV/Å per atom. The slabs were separated by a 20.41 Å vacuum in the *z* direction. A Gamma k-

points mesh was set to be 4×4×2. The electronic exchange-correlation interaction along with the GGA functional in the parameterization of the Perdew Burke and Ernzerhof (PBE) pseudopotential were analyzed by the projector augmented wave (PAW) potentials. The wave function with a cut off energy of 500 eV was represented by a plane wave. Importantly, the long-range interactions (DFT-D3) were recognized as a correction in all calculations. The DFT+U method was used to adjust the strongly correlated interaction of d electrons and the *U*-*J* value of Mo element was set to 2.0 eV. The diffusion pathways and energetics of Zn²⁺ diffusion throughout the bulk of MoS₂ were calculated through climbing image nudged elastic band (CINEB) method. Specifically, the minimum energy paths (MEP) in the CINEB procedure were initialized by linear interpolation of 4 images between the two fully relaxed end-point geometries, and each image was converged to <10⁻⁵ eV per super cell.

3 Results and discussion

It is well known that molybdenum disulfide (MoS₂) is characterized by a typical layer structure consisting of two S atomic planes and a Mo plane, and the interlayer distance of pure MoS₂ is about 6.2 Å [37]. As one of the most stable layer transition-metal dichalcogenides, MoS₂ can also exhibit considerable Zn²⁺ storage capability. However, due to the large electrostatic interaction between the intercalated divalent Zn²⁺ and the anions/cations in host material, the various Zn²⁺ storage performance of MoS₂ can be observed *via* regulating its host structure. For instance, after intercalating different guest species, MoS₂ shows outstanding electrochemical performance with improved electronic structure [37–40]. The reason why the electronic conductivity vary according to high quality intercalation can be explained as the interlayer van der Waals gap is expanded along with the deep intercalation of different guest species. Meanwhile, the oxidation state of Mo is usually changed with the transition of semiconducting 2H to metallic 1T phase [41,42].

According to the previous report about crystal water boosting desirable aqueous zinc ions storage performance of MoS₂@H₂O cathode [43], it can be found that MoS₂ is equipped with the natural ability of assimilating a certain number of solvent molecules into its inner layer structure. Therefore, the rational hypothesis of co-intercalating water and EG molecules into layer space of MoS₂ for the generation of novel MoS₂@EG anode come into being. From the result of XRD patterns (Figure 1g), it can be observed that the (002) peak of pure MoS₂ matches accurately with the hexagonal 2H-MoS₂ phase (JCPDS No. 37-1492) because of the successful removal of interlayer crystal water. And the

(002) peak of $\text{MoS}_2@H_2O$ shifts to a lower degree (2θ) than pure MoS_2 , indicating that the layer distance is expanded. Notably, for the as-prepared $\text{MoS}_2@EG$, with a diploid relationship, two new peaks index to (002) and (004) crystalline planes at about 9.3° and 18.6° , respectively, which can be signals of layer distance of 9.5 \AA and the further expanded interlayer van der Waals gap [37,38]. Compare with $\text{MoS}_2@H_2O$, the larger layer distance of $\text{MoS}_2@EG$ might result from the co-intercalation of water and EG molecules, and similar phenomenon of intercalating small organic molecules including EG into MoS_2 were reported previously [35,44–46]. To confirm the co-existence of water and EG, the Fourier transform infrared (FTIR) spectroscopy was utilized. As shown in Figure 1h, the peaks at $2,934$ and $2,874 \text{ cm}^{-1}$ are attributed to C–H bonds and the peak at 867 cm^{-1} should be assigned to C–C bonds [44,47]. While the peaks at around $1,397$ and 702 cm^{-1} are only appearing in $\text{MoS}_2@EG$ and $\text{MoS}_2@H_2O$ but not in pure MoS_2 [43]. The above FTIR results suggest that $\text{MoS}_2@EG$ displays the similar structural characteristic as $\text{MoS}_2@H_2O$ and exhibits unique FTIR features derived from the existence of EG, which can firmly demonstrate the existence of EG in $\text{MoS}_2@EG$. Besides, the TGA curves reveal the content of physically absorbed water is about 6.34%, and $\text{MoS}_2@EG$ shows a similar thermal evaporation process as $\text{MoS}_2@H_2O$ (Figure 1i). In the end, the weight loss of $\text{MoS}_2@EG$ (12.42%) is close to that of $\text{MoS}_2@H_2O$ (13.09%). Coupled with the XRD results derived from the powder after-TGA treatment (Figure S1), it can be thought that the relative lower weight loss of $\text{MoS}_2@EG$ might be caused by the preservation of the interlayered EG after heat treating of TGA, and such thermodynamic behavior may be beneficial to the structural stability of $\text{MoS}_2@EG$. Deeply, the result of the selective-area elemental analysis implies that the atomic ratios of Mo, S, O and C in the established part of $\text{MoS}_2@EG$ are about 21.65%, 42.84%, 31.69% and 3.82%, respectively (Figures S2 and S3), reflecting that the weight of EG in $\text{MoS}_2@EG$ is about 2.96%.

Although the dominant occupation for total interlayered intercalants in $\text{MoS}_2@EG$ is crystal water, the small number of EG molecules can influence both physical and chemical characteristics of $\text{MoS}_2@EG$. For instance, the distinct morphology is related to the synthesize environment and composition of electrode material. As shown in Figure 1e, though the $\text{MoS}_2@EG$ displaying the same blooming flowers shape as $\text{MoS}_2@H_2O$ (Figure S4b), the particles of $\text{MoS}_2@EG$ are slightly larger and denser, possibly contributing to robust electrochemical cycling. Then, the microstructure characteristics of $\text{MoS}_2@EG$ were determined *via* TEM images (Figure 1f and Figure S5). The observed interplanar distance of 9.5 and 4.8 \AA can be consistent with (002) and (004) crystalline plane of $\text{MoS}_2@EG$, respectively. The elemental mapping in Figure 1j represent the Mo, S, O and C

are evenly distributing at the surface of $\text{MoS}_2@EG$ particles.

The respective electrochemical performances of MoS_2 , $\text{MoS}_2@H_2O$ and $\text{MoS}_2@EG$ were examined through fabricating CR-2032-type half-cells including Zn foil counter electrodes. The obtained five cyclic voltammetry (CV) curves between 0.2 and 1.25 V (*vs.* Zn^{2+}/Zn) at 0.1 mV s^{-1} are shown in Figure 2a and Figure S7. Clearly, the lowest intensity of response current among these three samples indicates the negligible Zn^{2+} storage capability for pure MoS_2 (Figure S7a), which is consistent with the results reported previously [37,38,40,43]. Almost no redox peaks can be found in the whole CV results, corresponding to low electrochemical activity for MoS_2 in aqueous ZIB system visually. Then, the obvious redox peaks locate at around $0.68/1.1 \text{ V}$ (*vs.* Zn^{2+}/Zn) show that the larger layer distance is contributing to exploiting the Zn^{2+} -intercalation potential for $\text{MoS}_2@H_2O$ as a host material (Figure S7b). To further enlarge the interlayer distance, the as-synthesized $\text{MoS}_2@EG$ with multi-intercalants containing water and EG can provide more spacious room to accommodate more Zn^{2+} ions. Therefore, the CV curves of $\text{MoS}_2@EG$ show strongest intensity of response current (Figure 2a), indicating the higher capacity than $\text{MoS}_2@H_2O$ and MoS_2 . Interestingly, the broad redox peaks might signify the prominent intercalation pseudocapacitance induced by the optimized desolvation reaction of $\text{MoS}_2@EG$. In addition, an inconspicuous anodic peak at about 0.38 V (*vs.* Zn^{2+}/Zn) during charging process should be assigned to a part of Zn^{2+} ions deintercalation [38,39,43,48]. Consequently, the $\text{MoS}_2@EG$ electrode should possess high capacity and high-rate performance based on the above results.

Figure 2b displays the cycling performance of these three electrodes at 0.2 A g^{-1} . The $\text{MoS}_2@EG$ delivers an initial discharge capacity of 166.2 mAh g^{-1} with the high Coulombic efficiency of 93.2%. After 50 cycles, $\text{MoS}_2@EG$ still maintains the reversible capacity of 152.4 mAh g^{-1} , corresponding to the high capacity retention of 91.7%. While the low reversible capacity of 85.8 mAh g^{-1} for $\text{MoS}_2@H_2O$ verifies the enhanced electrochemical performance of $\text{MoS}_2@EG$ firmly. The corresponding charge and discharge profiles are provided in Figure S8. Visually the $\text{MoS}_2@EG$ can keep more stable voltage-output than $\text{MoS}_2@H_2O$ during cycling performance, demonstrating the smaller polarization and higher structural stability of $\text{MoS}_2@EG$ electrode. The rate performances in Figure 2c suggest the superior rate performance of $\text{MoS}_2@EG$ at different current densities (Figure S9). As a result, the capacities of 148.5 , 140.1 , 130.1 , 119.7 , 108.1 , 87.0 and 70.0 mAh g^{-1} at 0.1 , 0.2 , 0.5 , 1 , 2 , 5 and 10 A g^{-1} , respectively, are delivered by $\text{MoS}_2@EG$, while $\text{MoS}_2@H_2O$ shows 115.2 , 104.4 , 91.1 , 81.4 , 71.1 , 58.2 and 44.4 mAh g^{-1} and MoS_2 displays negligible capacities at the same current densities. When the current recovers to the low density of 0.1 A g^{-1} , the delivered capacity of 159.3

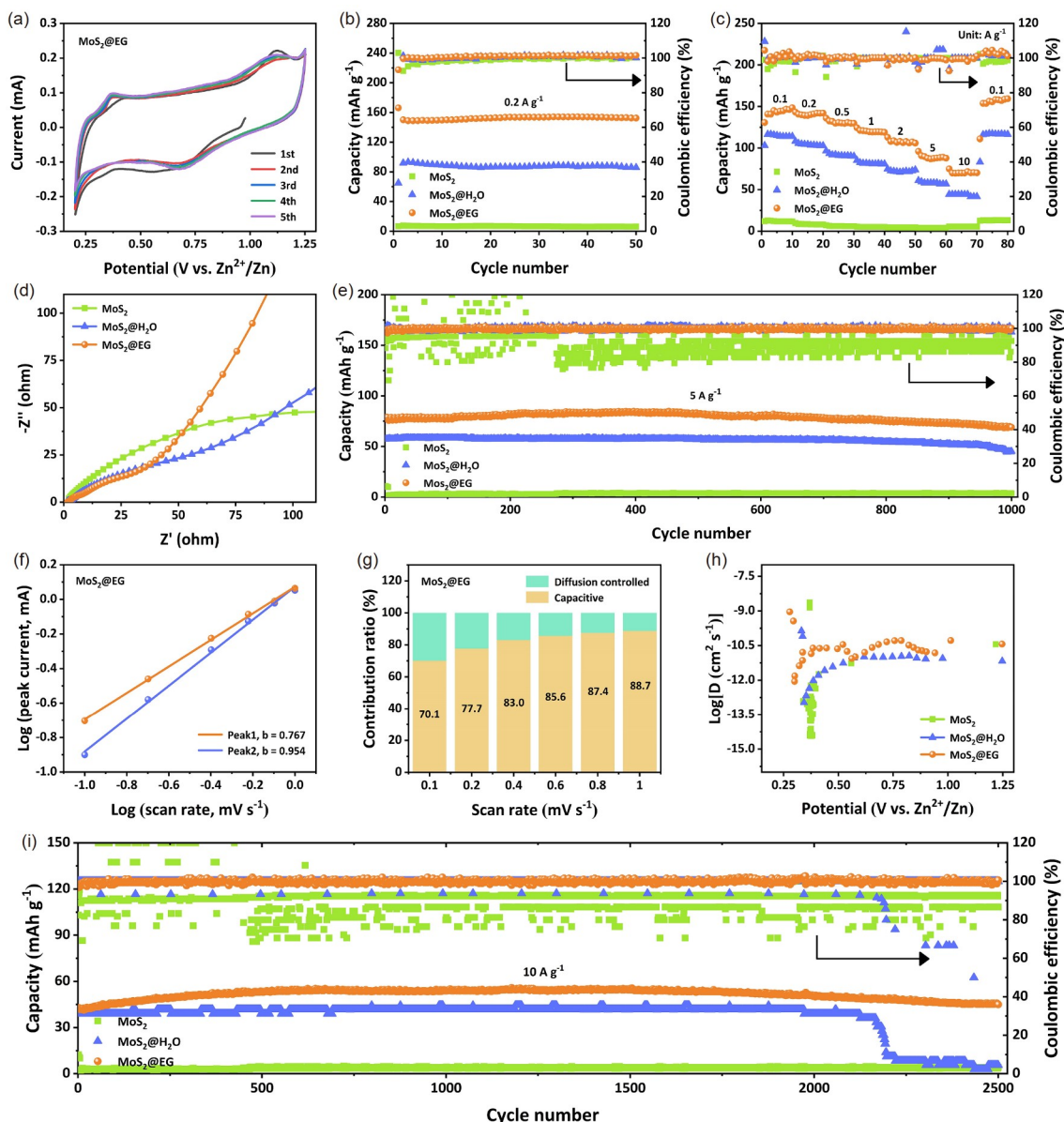


Figure 2 (a) CV curves of MoS₂@EG electrodes at 0.1 mV s⁻¹ between 0.2 and 1.25 V (vs. Zn²⁺/Zn). (b) Cycling and (c) rate performances of MoS₂, MoS₂@H₂O and MoS₂@EG. (d) EIS of the MoS₂, MoS₂@H₂O and MoS₂@EG electrodes. Long-term cycling performance of the MoS₂, MoS₂@H₂O and MoS₂@EG electrodes at (e) 5 A g⁻¹ and (i) 10 A g⁻¹. (f) The *b* values of MoS₂@EG electrode. (g) The calculated capacitive contribution ratios of MoS₂@EG electrode. (h) The $D_{Zn^{2+}}$ value of MoS₂, MoS₂@H₂O and MoS₂@EG electrodes (color online).

mAh g⁻¹ for MoS₂@EG is higher than its initial state. In fact, this phenomenon also occurs in both MoS₂@H₂O and MoS₂, which can be ascribed to the activation process during repeated cycling performance [38]. To understand the distinct high-rate performance for MoS₂@EG, the electrochemical impedance spectra (EIS) measurements were conducted at the fully charged state after 5 cycles. As shown in Figure 2d, the smallest radius of semi-circle represents the highest electronic conductivity of MoS₂@EG. Besides, the EIS tests were further carried out after different cycles for MoS₂@EG. In Figure S10, the interfacial charge-transfer resistance reflected by the size of semi-circle fluctuates at a narrow range

between about 50 and 150 Ω within 1,000-cycles electrochemical cycling performance, implying the reliable interfacial stability and relative high reversibility for MoS₂@EG. As expected, MoS₂@EG electrode exhibits the highest reversible capacity of 69.1 mAh g⁻¹ with a capacity retention of 87.9% after 1,000 cycles at 5 A g⁻¹ (Figure 2e and Figure S11), while 45.0 mAh g⁻¹ is retained after 2,500 cycles without obvious capacity decay at 10 A g⁻¹ (Figure 2i and Figure S12).

The remarkable high-rate capability of MoS₂@EG may be derived from the intrinsic enlarged layer distance, low interface desolvation energy and enhanced electronic con-

ductivity. From the point of experiment, the reaction mechanism can be explored *via* the CV results based on different scan rates (Figure S13). The positions of redox peaks change with different scan rates due to the effect of electrochemical polarization. According to $i_p = av^b$, the linear relationships determined by peak current (i_p) and scan rate (v) are revealed in Figure 2f and Figure S14. The b value is utilized to judge whether the diffusion-control process or capacitive behavior playing the dominant role for the whole cycling performance [38]. Finally, the b values of MoS₂@EG are 0.767 and 0.954 for Peak 1 and Peak 2, respectively, which are higher than both MoS₂@H₂O and MoS₂ and tend to close to the value of 1. Hence, the MoS₂@EG electrode should possess prominent pseudocapacitive behavior. And the reaction kinetics of MoS₂@EG is analyzed through the equation of $i(V) = k_1v + k_2v^{1/2}$ quantitatively (Figure 2g), where $i(V)$ is the specific response current at the corresponding potential, the k_1v and $k_2v^{1/2}$ are the components corresponding to capacitive and diffusion-controlled processes, respectively. Consequently, the capacitive contribution ratios of MoS₂@EG electrode are 70.1%, 77.7%, 83.0%, 85.6%, 87.4% and 88.7% at 0.1, 0.2, 0.4, 0.6, 0.8 and 1 mV s⁻¹, respectively. In addition to the dominant capacitive behavior, the Zn²⁺ diffusion rate might also promote the fast reaction kinetics. As a result, the calculated $D_{Zn^{2+}}$ value of around 10⁻⁹–10⁻¹² cm² s⁻¹ for MoS₂@EG is slightly larger than that of both MoS₂@H₂O and MoS₂ (Figure 2h and Figure S15). Based on the above results, it can be concluded that the MoS₂@EG electrode with low desolvation resistance possesses the advantages of fast Zn²⁺ diffusion rate and outstanding pseudocapacitive behavior, thereby promoting the high-rate performance.

Recently, the sulfur vacancies modified MoS₂ can maintain its layer structure without expansion or shrinking during electrochemical cycling tests because Zn²⁺ ions are mainly intercalating into edge and vacancy sites instead of the interlayer planes [4]. Nevertheless, most reported enlarged-interlayer-space MoS₂ cathodes tend to widen layer distance during Zn²⁺ ions intercalation process, and then the size of interlayer distance recovers back to the pristine state after deintercalation reaction [36–39,43,48–50]. In general, the interlayer space of MoS₂ should be enlarged after the Zn²⁺ intercalation because a certain amount of the intercalated zinc ions will further cut down the weak interlayer van der Waals' forces of MoS₂. As shown in Figure S16, the interlayer distance of MoS₂@H₂O electrode increases from 8.0 to 9.0 Å during the discharge process, and then recovers to 8.0 Å at the fully charge state. Conversely, MoS₂@EG electrode experiences the structural shrinking during Zn²⁺ intercalation process, which is different from the previous reported MoS₂ and MoS₂@H₂O electrodes. Through *ex-situ* XRD technology (Figure 3b), it can be seen that the

(002) peak of MoS₂@EG shifts to the larger degree gradually during initial discharge process (A–D) (Figure S17), suggesting the interlayer distance is decreasing from 9.5 to 9.0 Å. Then, the layer structure recovers to the originated state from D to G. Subsequently, the (002) peak moves reversibly in the second (G–I) and third (I–K) cycling tests, corresponding to the reversible structural shrinking characteristic of MoS₂@EG. Furthermore, the *ex-situ* XPS characterizations (Figure S18) were conducted to analyze the phase transition of MoS₂@EG during charge and discharge processes. Theoretically, Zn²⁺ ions intercalate into MoS₂ with electrons donation to form Zn_xMoS₂, thereby promoting the 2H to 1T phase transition along with improving the electronic conductivity of MoS₂ electrode [42]. Therefore, the contents of 1T phase increases with decreasing 2H phase at fully discharging state (Figure 3c), corresponding to the phase transition from 2H to 1T. Reversibly, the 1T phase transforms to 2H phase at fully charging state. Meanwhile, the proportion variety of 2H phase keeps high reversibility, which is conducive to the structural stability of MoS₂@EG. Besides, it is worth noting that the metastable 1T phase is easy to be oxidized, so the content of Mo⁶⁺ increases dramatically at the initial cycle and then maintains at a relative constant level during the subsequent cycling tests. These *ex-situ* characterization results reveal that MoS₂@EG undergoes the structural shrinking with increasing content of 1T phase during Zn²⁺ ions intercalation, and recovers to its originated state at deintercalation process, confirming the optimized 2D structure of MoS₂@EG is stable and the electronic structure of MoS₂@EG is also changing with the phase transition between 1T and 2H phases.

For hexagonal 2H-MoS₂, the E_{2g}¹ (≈310 cm⁻¹) and A_{1g} (≈330 cm⁻¹) peaks are ascribed to in-plane and out-of-plane vibrations, respectively, while the J₁ (≈157 cm⁻¹) and J₂ (≈177 cm⁻¹) correspond to the vibration modes of trigonal 1T-MoS₂ phase. As shown in Figure 3e (Figure S19), the intensity of 2H phase decrease gradually and the 1T phase enhanced simultaneously during the discharge process, then, the 1T phase transform to the 2H phase during the charge process. The intensities of both 2H and 1T phases can not recover to the pristine state at the fully charge state because the irreversible intercalated Zn²⁺ ions are trapped in MoS₂@EG at initial discharge and charge processes. In addition, the intensity ratio of A_{1g}/E_{2g}¹ decreases from ≈1.6 to ≈1.0 (Figure 3f), evidencing the Zn²⁺ ions intercalate into MoS₂@EG electrode [38]. And the values of A_{1g}/E_{2g}¹ recover to ≈1.5 after fully charging process, corresponding to Zn²⁺ ions de-intercalation process. The dynamic change of A_{1g}/E_{2g}¹ value demonstrates the reversible Zn²⁺ ion storage process of MoS₂@EG electrode firmly.

More deeply, DFT calculations were implemented to study

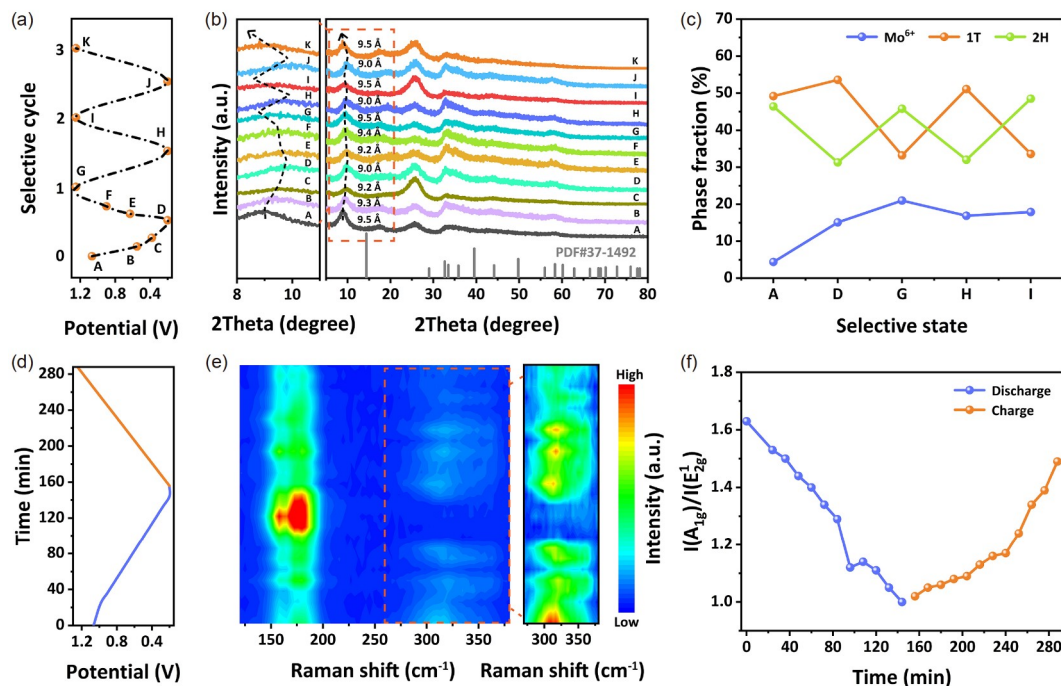


Figure 3 (a) The different voltage states correspond to the *ex-situ* XRD and XPS patterns. (b) *Ex situ* XRD patterns of the MoS₂@EG electrodes collected at initial three cycles. (c) The dynamic phase transition of the MoS₂@EG electrodes during charge/discharge processes. (e) The *in situ* electrochemical Raman spectra and (d) the corresponding voltage states. (f) The intensity ratio of A_{1g}/E_{2g}¹ at different voltage states (color online).

the charge storage mechanism of MoS₂@EG electrode theoretically. Firstly, the calculated total density of states (DOS) in Figure 4a–c show that MoS₂@EG possesses the highest electronic conductivity, which is consistent with the experimental results based on the EIS test. Secondly, the calculation results of intercalation formation energy demonstrate that Zn²⁺ ions can intercalate into MoS₂@EG more easily because of the more favorable intercalation formation energy of -3.32 eV for MoS₂@EG than that of MoS₂@H₂O (-1.92 eV) (Figure 4d). This may be attributed to the interlayer interaction between the intercalated Zn²⁺ ions and EG molecules, thereby facilitating the desolvation process of [Zn(H₂O)₆]²⁺ and achieving fast interlayer Zn²⁺ conductivity. Specifically, due to the given host of 2H phase MoS₂, the intercalated Zn²⁺ ions diffuse with the same diffusion pathway in MoS₂, MoS₂@H₂O and MoS₂@EG, as displayed in Figure 4e. However, the diffusion barrier between adjacent sites is 0.1048 eV in MoS₂@EG, which is obviously lower than MoS₂@H₂O (0.1215 eV) and MoS₂ (0.4441 eV) (Figure 4f). In order to analyze the distinct bonding behavior of Zn²⁺ ions in inner interlayer structure, differential charge density was figured out in Figure 4g–i. The charge accumulation is almost distributing over the whole interlayer space of MoS₂ (Figure 4g), resulting in the strong interaction between Zn²⁺ ion and the bulk of MoS₂, along with the sluggish Zn²⁺ diffusion in MoS₂. Interestingly, nearly a half of the interlayer binding interaction is weakened in MoS₂@H₂O and the interlayered water molecules can alle-

viate a part of electrostatic effect around the positive Zn²⁺ ion (Figure 4h), so that the stability of MoS₂@H₂O can be enhanced and Zn²⁺ also can diffuse quickly. Similarly, the EG molecules can further share the electrostatic interaction derived from the positive Zn²⁺ ion (Figure 4i), therefore, MoS₂@EG can be more stable and Zn²⁺ ion can also diffuse more easily with little interlayer constraints. Combined with the low diffusion barrier and weak interaction between Zn²⁺ ion and the bulk of MoS₂@EG, it is believed that different forms of hydrate Zn²⁺ ions may can intercalate into MoS₂@EG with low desolvation energy. The restricted interlayer electrostatic interaction between Zn²⁺ ions and MoS₂ host framework caused by co-intercalation of water and EG molecules should contribute to fast Zn²⁺ diffusion kinetics and improved cycling performance of MoS₂@EG.

Practically, to realize the rocking chair aqueous ZIB using MoS₂@EG anode, two styles of rocking chair aqueous ZIB including MoS₂@EG||Zn_xNVPF and MoS₂@EG||Zn_xPVO were fabricated successfully (Figure S20). Considering the distinguished rate performance of the polyaniline-intercalated V₂O₅ (PVO) [51], the MoS₂@EG anode is paired with PVO cathode, and a relative low output voltage of MoS₂@EG||Zn_xPVO full cell could be assessed at about 0.6 V (Figure S21). Remarkably, the high-rate capability of MoS₂@EG is unblocked in the MoS₂@EG||Zn_xPVO system, therefore, the MoS₂@EG||Zn_xPVO can exhibit 127.4, 122.1, 106.2, 88.0 and 76.4 mAh g⁻¹ at 1, 2, 5, 8 and 10 A g⁻¹, respectively (Figure 5a, b). Simultaneously, the MoS₂@EG||

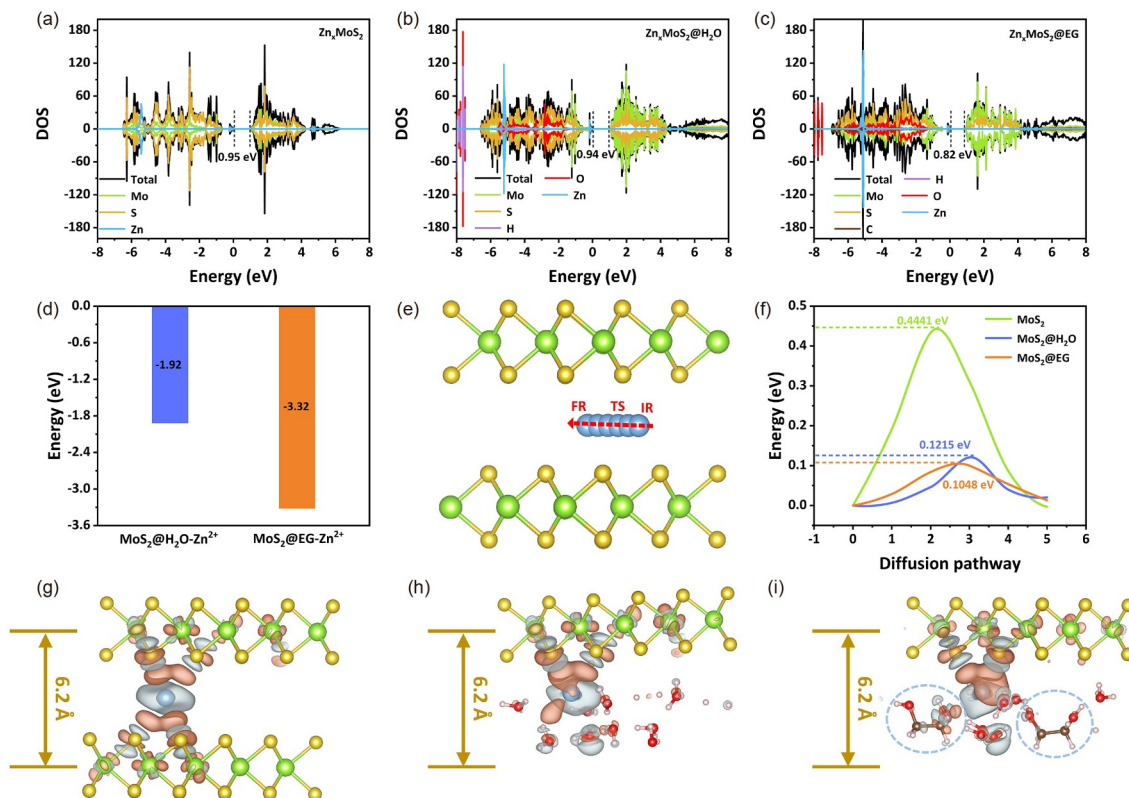


Figure 4 The calculated total density of states for (a) Zn_xMoS_2 , (b) $Zn_xMoS_2@H_2O$ and (c) $Zn_xMoS_2@EG$. (d) The intercalation formation energy of $MoS_2@H_2O$ and $MoS_2@EG$. (e) Diffusion pathway and (f) the corresponding diffusion barrier of Zn^{2+} in MoS_2 , $MoS_2@H_2O$ and $MoS_2@EG$. Differential charge density with Zn^{2+} intercalation in (g) MoS_2 , (h) $MoS_2@H_2O$ and (i) $MoS_2@EG$. The brown and grey represent charge accumulation and depletion, respectively. Light blue, yellow, green, dark brown, red and white balls represent Zn, S, Mo, C, O and H atoms, respectively (color online).

Zn_xPVO system also shows stable cycling performance, a high reversible capacity of 122.8 mAh g^{-1} is maintained at 2 A g^{-1} after 2,000 cycles with the capacity retention of nearly 100% (Figure 5c). Furthermore, the $MoS_2@EG||Zn_xPVO$ can retain 75.0 mAh g^{-1} with the corresponding capacity retention of 86.9% after 20,000 cycles at 5 A g^{-1} (Figure S22), and the ultra-durable performance with 100,000 cycles is achieved at 10 A g^{-1} (Figure 5d), implying the great compatibility between $MoS_2@EG$ anode and PVO cathode is reached.

However, the low working potential of $MoS_2@EG||Zn_xPVO$ full battery is unfavorable to the development for high-voltage aqueous ZIB systems. Figure S23 shows the typical charging and discharging profiles of $MoS_2@EG$ anode and $Na_3V_2(PO_4)_2O_2F$ (NVPF) cathode, and a higher output voltage of $\approx 1.0 \text{ V}$ for $MoS_2@EG||Zn_xNVPF$ full cell could be estimated approximately. In Figure S25, the $MoS_2@EG||Zn_xNVPF$ delivers 131.8, 95.1, 81.3, 73.3 and 54.1 mAh g^{-1} at 0.2, 0.5, 0.75, 1 and 2 A g^{-1} , respectively, and the corresponding charging/discharging curves are displayed in Figure S24. Thanks to the stable crystal structure of NVPF [52], $MoS_2@EG||Zn_xNVPF$ system with superior stability shows a reversible capacity of 100.0 mAh g^{-1} after 200 cycles at 0.2 A g^{-1} (Figure S26), and a capacity retention of 79.9%

after 9,000 cycles can be obtained at 1 A g^{-1} (Figure 5e). As a result, the rechargeable high-voltage $MoS_2@EG||Zn_xNVPF$ and high-rate $MoS_2@EG||Zn_xPVO$ rocking chair full cells indicate the $MoS_2@EG$ anode as a suitable Zn^{2+} host material possesses huge potential to replace Zn metal.

To promote the practicality of applying $MoS_2@EG$ anode for assembling Zn-metal-free rocking chair Zn-ion batteries, the low-temperature performance of $MoS_2@EG||Zn$ half cell and $MoS_2@EG||Zn_xNVPF$ full battery were examined at $-20 \text{ }^\circ\text{C}$. Generally, high ion conductivity tends to emerging at high temperature, Zn^{2+} ions conductivity should decrease at low-temperature aqueous electrolyte, which will limit the high-rate performance. Encouragingly, $MoS_2@EG||Zn$ half cell can display 76.7 mAh g^{-1} after 200 cycles at 0.1 A g^{-1} (Figure S27). This outstanding low-temperature tolerance could be attributed to the low required desolvation energy before Zn^{2+} intercalation into $MoS_2@EG$. Then, Figure 5g displays the low-temperature cycling performance of $MoS_2@EG||Zn_xNVPF$ full battery at 0.2 A g^{-1} . Unexpectedly, $MoS_2@EG||Zn_xNVPF$ full battery sustains 50.5 mAh g^{-1} within 1,300 cycles at 0.2 A g^{-1} , the limited capacity may be resulted from the intrinsic low electronic conductivity of NVPF cathode [52]. Simultaneously, the electrochemical polarization of $MoS_2@EG||Zn_xNVPF$ is close to the results at

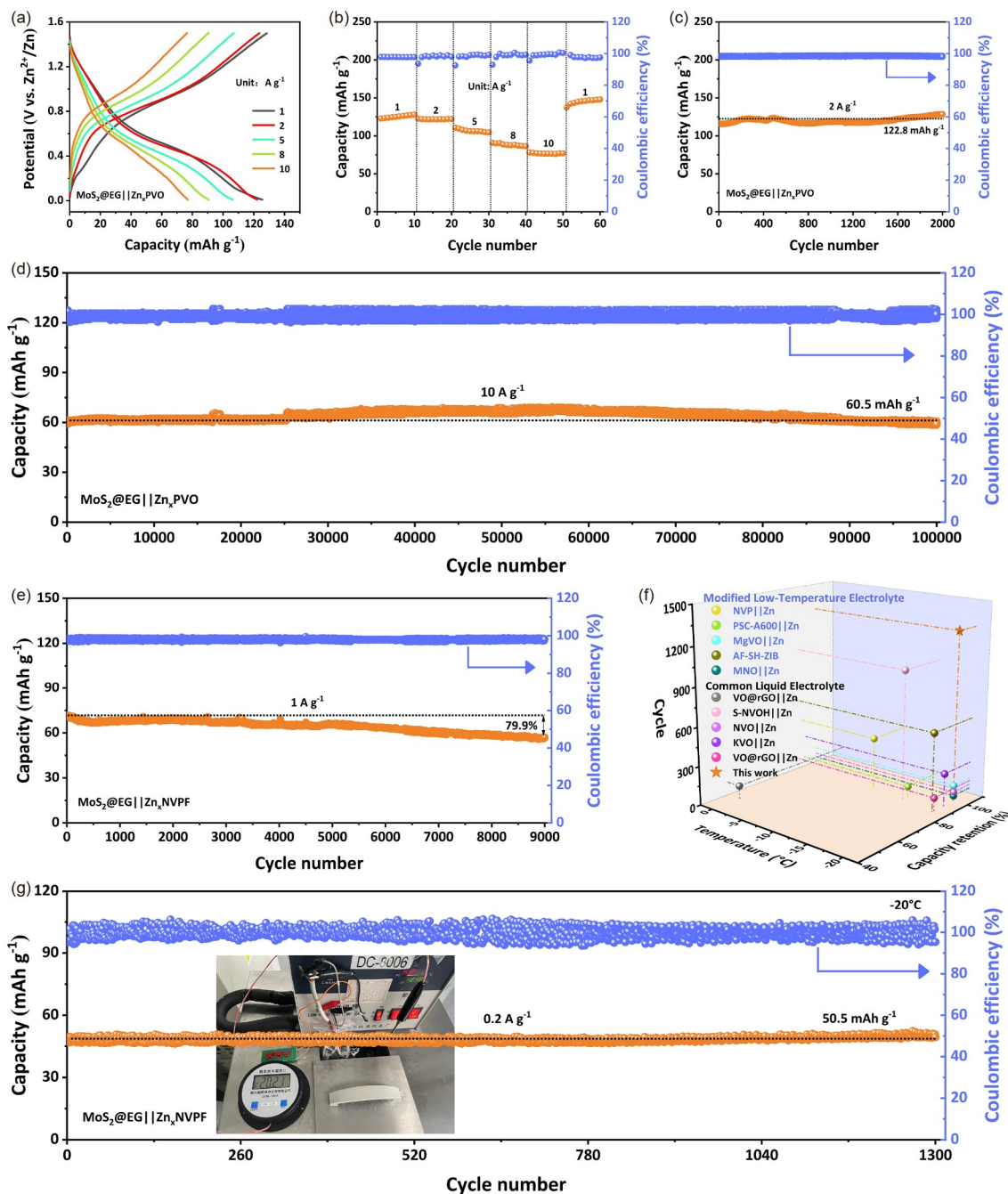


Figure 5 (a) Charge-discharge profiles of $\text{MoS}_2@\text{EG}||\text{Zn}_x\text{PVO}$ full cell at different current densities. (b) Rate performance of $\text{MoS}_2@\text{EG}||\text{Zn}_x\text{PVO}$ rocking chair aqueous ZIBs. Cycling performance of $\text{MoS}_2@\text{EG}||\text{Zn}_x\text{PVO}$ at (c) 2 A g^{-1} and (d) 10 A g^{-1} . (e) Long-term stability of $\text{MoS}_2@\text{EG}||\text{Zn}_x\text{NVPF}$ at 1 A g^{-1} . (f) The comparison between the $\text{MoS}_2@\text{EG}||\text{Zn}_x\text{NVPF}$ full battery and other Zn-metal based ZIBs in terms of cycle life at low temperature. (g) Low-temperature tolerance of $\text{MoS}_2@\text{EG}||\text{Zn}_x\text{NVPF}$ systems at -20°C (color online).

room temperature (Figure S28), demonstrating the strong low-temperature tolerance of $\text{MoS}_2@\text{EG}||\text{Zn}_x\text{NVPF}$ rocking chair full cell system. Actually, the performance at low temperature for ZIBs mainly relies on the ion conductivity in electrolyte and ion diffusion rate in the bulk of electrode [53]. The polyanion-type NVPF cathode possesses special 3D framework composed of PO_4 tetrahedrons and VO_6 octahedrons, contributing to providing stable ion channels for

fast ions transport [52], therefore, the $\text{MoS}_2@\text{EG}||\text{Zn}_x\text{NVPF}$ full battery shows high cycling stability at -20°C . Besides, to ameliorate the anti-freezing characteristics of aqueous electrolyte, many works focus on introducing electrolyte additives or fabricating hydrogel electrolytes. Nevertheless, the stable performance of $\text{MoS}_2@\text{EG}||\text{Zn}_x\text{NVPF}$ full battery is realized *via* $4 \text{ M Zn}(\text{CF}_3\text{SO}_3)_2$ electrolyte without any additives directly, and the low-temperature performance of

MoS₂@EG||Zn_xNVPF full cell can still be better than many other Zn-metal based ZIBs [54–57], and even be superior to that of ZIBs using modified low-temperature electrolyte (Figure 5f) [58–62]. Nowadays, many reports have demonstrated that the electrolyte additives can improve ion conductivity of electrolyte at low temperature effectively [53,63]. Hence, the low-temperature electrochemical performance of MoS₂@EG-based Zn-metal-free rocking chair Zn-ion batteries may be improved through searching for suitable cathodes, optimizing the components of aqueous electrolyte and exploring the relationship between the structure of MoS₂ and low-temperature performance.

4 Conclusions

In conclusion, the novel MoS₂@EG anode with low required interface desolvation energy exhibits prominent pseudocapacitive behavior, showing high-rate performance and higher capacity than MoS₂@H₂O and pure MoS₂. The DFT calculation reveals that the EG and crystal water molecules can alleviate a certain part of the electrostatic interaction between the intercalated Zn²⁺ ion and the MoS₂@EG host framework, so the Zn²⁺ can diffusion quickly and the structural stability of MoS₂@EG can be improved. The *ex-situ* and *in-situ* characterization results indicate that the MoS₂@EG electrode can not only store Zn²⁺ ions with high reversibility, but also undergo the reversible phase transition between 1T and 2H MoS₂ simultaneously. The MoS₂@EG||Zn_xNVPF full cell with a high output voltage of ≈1.0 V shows considerable stability, and the MoS₂@EG||Zn_xPVO full battery displays high-rate performance, highlighting the MoS₂@EG anode possesses great attraction to replace Zn metal for rocking chair ZIBs. Moreover, the feasible low-temperature performance of MoS₂@EG||Zn_xNVPF system is demonstrated. However, due to the limitations of low ion conductivity in electrolyte and degeneration of ion diffusion in the bulk of electrode, the low-temperature performance of aqueous rocking chair ZIBs should be improved further through effective strategy of optimizing the component of aqueous electrolyte and the structure of electrode.

Acknowledgements This work was supported by the National Natural Science Foundation of China (22109030, 22021001), the Fundamental Research Funds for the Central Universities (20720220073), the Key Research and Development Program of Yunnan Province (202103AA080019), the Fujian Industrial Technology Development and Application Plan (202210002) and the Guangdong Basic and Applied Basic Research Foundation (2019A1515111069, 2021A1515010177). Dr. Yufei Zhang gratefully acknowledge the financial support from Guangdong Basic and Applied Basic Research Foundation (2020A1515010886). The authors acknowledge Beijing PARATERA Tech CO., Ltd. for providing HPC resources that have contributed to the research results reported within this paper. URL: <https://paratera.com/>.

Conflict of interest The authors declare no conflict of interest.

Supporting information The supporting information is available online at chem.scichina.com and link.springer.com/journal/11426. The supporting materials are published as submitted, without typesetting or editing. The responsibility for scientific accuracy and content remains entirely with the authors.

- 1 Wang G, Wang Y, Guan B, Liu J, Zhang Y, Shi X, Tang C, Li G, Li Y, Wang X, Li L. *Small*, 2021, 17: 2104557
- 2 Liu N, Wu X, Zhang Y, Yin Y, Sun C, Mao Y, Fan L, Zhang N. *Adv Sci*, 2020, 7: 2000146
- 3 Yang Y, Tang Y, Fang G, Shan L, Guo J, Zhang W, Wang C, Wang L, Zhou J, Liang S. *Energy Environ Sci*, 2018, 11: 3157–3162
- 4 Zhou J, Wu F, Mei Y, Hao Y, Li L, Xie M, Chen R. *Adv Mater*, 2022, 34: 2200782
- 5 Zheng J, Huang Z, Zeng Y, Liu W, Wei B, Qi Z, Wang Z, Xia C, Liang H. *Nano Lett*, 2022, 22: 1017–1023
- 6 Yan J, Ye M, Zhang Y, Tang Y, Chao Li C. *Chem Eng J*, 2022, 432: 134227
- 7 Wang Y, Guo T, Yin J, Tian Z, Ma Y, Liu Z, Zhu Y, Alshareef HN. *Adv Mater*, 2022, 34: 2106937
- 8 Wang W, Huang G, Wang Y, Cao Z, Cavallo L, Hedhili MN, Alshareef HN. *Adv Energy Mater*, 2022, 12: 2102797
- 9 Yang Y, Liu C, Lv Z, Yang H, Zhang Y, Ye M, Chen L, Zhao J, Li CC. *Adv Mater*, 2021, 33: 2007388
- 10 Yang Y, Liu C, Lv Z, Yang H, Cheng X, Zhang S, Ye M, Zhang Y, Chen L, Zhao J, Li CC. *Energy Storage Mater*, 2021, 41: 230–239
- 11 Li C, Xie X, Liu H, Wang P, Deng C, Lu B, Zhou J, Liang S. *Nat Sci Rev*, 2022, 9: nwab177
- 12 Song Y, Ruan P, Mao C, Chang Y, Wang L, Dai L, Zhou P, Lu B, Zhou J, He Z. *Nano-Micro Lett*, 2022, 14: 218
- 13 Zhang S, Hao J, Luo D, Zhang P, Zhang B, Davey K, Lin Z, Qiao S. *Adv Energy Mater*, 2021, 11: 2102010
- 14 Han D, Wang Z, Lu H, Li H, Cui C, Zhang Z, Sun R, Geng C, Liang Q, Guo X, Mo Y, Zhi X, Kang F, Weng Z, Yang Q. *Adv Energy Mater*, 2022, 12: 2102982
- 15 Ma Y, Zhang Q, Liu L, Li Y, Li H, Yan Z, Chen J. *Nat Sci Rev*, 2022, 9: nwac051
- 16 Lv Z, Wang B, Ye M, Zhang Y, Yang Y, Li CC. *ACS Appl Mater Interfaces*, 2022, 14: 1126–1137
- 17 Wang B, Yan J, Zhang Y, Ye M, Yang Y, Li CC. *Adv Funct Mater*, 2021, 31: 2102827
- 18 Yang Y, Xiao J, Cai J, Wang G, Du W, Zhang Y, Lu X, Li CC. *Adv Funct Mater*, 2020, 31: 2005092
- 19 Yan L, Zeng X, Li Z, Meng X, Wei D, Liu T, Ling M, Lin Z, Liang C. *Mater Today Energy*, 2019, 13: 323–330
- 20 Li W, Ma Y, Li P, Jing X, Jiang K, Wang D. *Adv Energy Mater*, 2021, 11: 2102607
- 21 Zhang J, Lei Q, Ren Z, Zhu X, Li J, Li Z, Liu S, Ding Y, Jiang Z, Li J, Huang Y, Li X, Zhou X, Wang Y, Zhu D, Zeng M, Fu L. *ACS Nano*, 2021, 15: 17748–17756
- 22 Cheng Y, Luo L, Zhong L, Chen J, Li B, Wang W, Mao SX, Wang C, Sprenkle VL, Li G, Liu J. *ACS Appl Mater Interfaces*, 2016, 8: 13673–13677
- 23 Kaveevivitchai W, Manthiram A. *J Mater Chem A*, 2016, 4: 18737–18741
- 24 Chae MS, Hong ST. *Batteries*, 2019, 5: 3
- 25 He X, Zhang H, Zhao X, Zhang P, Chen M, Zheng Z, Han Z, Zhu T, Tong Y, Lu X. *Adv Sci*, 2019, 6: 1900151
- 26 Li W, Wang K, Cheng S, Jiang K. *Adv Energy Mater*, 2019, 9: 1900993
- 27 Xiong T, Zhang Y, Wang Y, Lee WSV, Xue J. *J Mater Chem A*, 2020, 8: 9006–9012
- 28 Cao J, Zhang D, Yue Y, Wang X, Srikrhaow A, Sriprachubwong C, Tuantranont A, Zhang X, Wu ZS, Qin J. *Chem Eng J*, 2021, 426:

- 131893
- 29 Wang X, Wang Y, Jiang Y, Li X, Liu Y, Xiao H, Ma Y, Huang Y, Yuan G. *Adv Funct Mater*, 2021, 31: 2103210
- 30 Chen X, Huang R, Ding M, He H, Wang F, Yin S. *ACS Appl Mater Interfaces*, 2022, 14: 3961–3969
- 31 Wen L, Wu Y, Wang S, Shi J, Zhang Q, Zhao B, Wang Q, Zhu C, Liu Z, Zheng Y, Su J, Gao Y. *Nano Energy*, 2022, 93: 106896
- 32 Yang B, Qin T, Du Y, Zhang Y, Wang J, Chen T, Ge M, Bin D, Ge C, Lu H. *Chem Commun*, 2022, 58: 1550–1553
- 33 Chou J, Zhao Y, Li X, Wang W, Tan S, Wang Y, Zhang J, Yin Y, Wang F, Xin S, Guo Y. *Angew Chem Int Ed*, 2022, 61: e202203137
- 34 Tan SJ, Tian YF, Zhao Y, Feng XX, Zhang J, Zhang CH, Fan M, Guo JC, Yin YX, Wang F, Xin S, Guo YG. *J Am Chem Soc*, 2022, 144: 18240–18245
- 35 Duan J, Qin G, Min L, Yang Y, Wang C. *ACS Appl Mater Interfaces*, 2018, 10: 38084–38092
- 36 Li C, Liu C, Wang Y, Lu Y, Zhu L, Sun T. *Energy Storage Mater*, 2022, 49: 144–152
- 37 Liang H, Cao Z, Ming F, Zhang W, Anjum DH, Cui Y, Cavallo L, Alshareef HN. *Nano Lett*, 2019, 19: 3199–3206
- 38 Li S, Liu Y, Zhao X, Shen Q, Zhao W, Tan Q, Zhang N, Li P, Jiao L, Qu X. *Adv Mater*, 2021, 33: 2007480
- 39 Li H, Yang Q, Mo F, Liang G, Liu Z, Tang Z, Ma L, Liu J, Shi Z, Zhi C. *Energy Storage Mater*, 2019, 19: 94–101
- 40 Xu W, Sun C, Zhao K, Cheng X, Rawal S, Xu Y, Wang Y. *Energy Storage Mater*, 2019, 16: 527–534
- 41 Lee C, Yan H, Brus LE, Heinz TF, Hone J, Ryu S. *ACS Nano*, 2010, 4: 2695–2700
- 42 Wang H, Lu Z, Xu S, Kong D, Cha JJ, Zheng G, Hsu PC, Yan K, Bradshaw D, Prinz FB, Cui Y. *Proc Natl Acad Sci USA*, 2013, 110: 19701–19706
- 43 Zhang Z, Li W, Wang R, Li H, Yan J, Jin Q, Feng P, Wang K, Jiang K. *J Alloys Compd*, 2021, 872: 159599
- 44 Jia B, Yu Q, Zhao Y, Qin M, Wang W, Liu Z, Lao CY, Liu Y, Wu H, Zhang Z, Qu X. *Adv Funct Mater*, 2018, 28: 1803409
- 45 Zheng N, Jiang G, Chen X, Mao J, Zhou Y, Li Y. *J Mater Chem A*, 2019, 7: 9305–9315
- 46 Cui Y, Liu W, Feng W, Zhang Y, Du Y, Liu S, Wang H, Chen M, Zhou J. *Adv Funct Mater*, 2020, 30: 1908755
- 47 Liang Y, Yoo HD, Li Y, Shuai J, Calderon HA, Robles Hernandez FC, Grabow LC, Yao Y. *Nano Lett*, 2015, 15: 2194–2202
- 48 Cao P, Chen N, Tang W, Liu Y, Xia Y, Wu Z, Li FZ, Liu Y, Sun A. *J Alloys Compd*, 2022, 898: 162854
- 49 Huang M, Mai Y, Zhao L, Liang X, Fang Z, Jie X. *ChemElectroChem*, 2020, 7: 4218–4223
- 50 Huang M, Mai Y, Fan G, Liang X, Fang Z, Jie X. *J Alloys Compd*, 2021, 871: 159541
- 51 Liu S, Zhu H, Zhang B, Li G, Zhu H, Ren Y, Geng H, Yang Y, Liu Q, Li CC. *Adv Mater*, 2020, 32: 2001113
- 52 Guo JZ, Wang PF, Wu XL, Zhang XH, Yan Q, Chen H, Zhang JP, Guo YG. *Adv Mater*, 2017, 29: 1701968
- 53 Liu Z, Luo X, Qin L, Fang G, Liang S. *Adv Powder Mater*, 2022, 1: 100011
- 54 Chen S, Zhang Y, Geng H, Yang Y, Rui X, Li CC. *J Power Sources*, 2019, 441: 227192
- 55 Su G, Chen S, Dong H, Cheng Y, Liu Q, Wei H, Ang EH, Geng H, Li CC. *Nanoscale*, 2021, 13: 2399–2407
- 56 Huang JQ, Lin X, Tan H, Du X, Zhang B. *J Energy Chem*, 2020, 43: 1–7
- 57 Zhang J, Wang M, Zeng M, Li X, Chen L, Yang Z, Chen J, Guo B, Ma Z, Li X. *J Power Sources*, 2021, 496: 229832
- 58 Li Z, Chen D, An Y, Chen C, Wu L, Chen Z, Sun Y, Zhang X. *Energy Storage Mater*, 2020, 28: 307–314
- 59 Xu W, Liu C, Ren S, Lee D, Gwon J, Flake JC, Lei T, Baisakh N, Wu Q. *J Mater Chem A*, 2021, 9: 25651–25662
- 60 Jin X, Song L, Dai C, Ma H, Xiao Y, Zhang X, Han Y, Li X, Zhang J, Zhao Y, Zhang Z, Duan L, Qu L. *Energy Storage Mater*, 2022, 44: 517–526
- 61 Liu S, Lei T, Song Q, Zhu J, Zhu C. *ACS Appl Mater Interfaces*, 2022, 14: 11425–11434
- 62 Geng H, Cheng M, Wang B, Yang Y, Zhang Y, Li CC. *Adv Funct Mater*, 2019, 30: 2070034
- 63 Liu D, Zhang Y, Liu S, Wei L, You S, Chen D, Ye M, Yang Y, Rui X, Qin Y, Li CC. *Adv Funct Mater*, 2022, 32: 2111714